


Cite this: *RSC Adv.*, 2017, 7, 18099

In situ construction of Z-scheme g-C₃N₄/Mg_{1.1}Al_{0.3}Fe_{0.2}O_{1.7} nanorod heterostructures with high N₂ photofixation ability under visible light

Yanjuan Wang, Wenshi Wei, Mengyan Li, Shaozheng Hu, * Jian Zhang* and Ruijiang Feng

By tuning the metal ratio, a Z-scheme g-C₃N₄/MgAlFeO nanorod composite was prepared *in situ*. The nitrogen photofixation performance under visible light was tested to evaluate the performance of the prepared catalysts. Strong electronic coupling, as evidenced by the XPS, PL and EIS results, exists between the two components in the g-C₃N₄/Mg_{1.1}Al_{0.3}Fe_{0.2}O_{1.7} heterojunction photocatalysts, leading to a more effective separation of photogenerated electron-hole pairs and faster interfacial charge transfer, causing the higher activity and stability for N₂ photofixation. Neat MgAlFeO shows almost no N₂ photofixation activity. However, with the MgAlFeO mass percentage of 23.6%, the as-prepared heterojunction photocatalyst exhibits the highest NH₄⁺ generation rate under visible light, which is 3.5-fold greater than that of individual g-C₃N₄. A possible Z-scheme mechanism is proposed.

Received 4th January 2017
Accepted 18th March 2017

DOI: 10.1039/c7ra00097a

rsc.li/rsc-advances

Introduction

Nitrogen is the main ingredient of many important organic compounds in plants. Nitrogen can directly affect the metabolism and growth of all living bodies. Since nitrogen is unusable in its molecular form to most organisms because of its strong nonpolar N≡N covalent triple bond, nitrogen fixation as ammonia is a significant important chemical process in nature. Ammonia is very extensively used in people's daily lives, including as chemical raw materials, fertilizers and refrigerants. However, the biochemical N₂ fixation process, which occurs with the help of specialized microorganisms, does not satisfy the increased demand of human beings. During the early 20th century, Haber invented the artificial nitrogen fixation method, the Haber-Bosch process, using hydrogen gas and nitrogen gas as raw materials in the presence of Fe-based catalysts under high pressure and temperature. Both the energy consumption and raw material costs are high for this process. Therefore, artificial nitrogen fixation using cheap raw materials under mild conditions is of considerable significance from the perspectives of cost and environmental protection. With this background, various methods have been developed, including chemical,^{1,2} electrochemical^{3,4} and photochemical routes.^{5,6}

In 1977, the process of N₂ reduction to NH₃ over Fe doped TiO₂ was discovered by Schrauzer *et al.*⁵ Since then, nitrogen photofixation technology becomes a hotspot and is considered to be a promising method to replace the traditional Haber-

Bosch process. Because of the poor visible light absorption, the traditional Ti-based semiconductor catalysts show unsatisfactory nitrogen fixation ability under visible light.⁷⁻⁹ In recent years, many novel nitrogen-photofixation catalysts are reported successively, including BiOBr (BiOCl), g-C₃N₄, multi-metal sulfide and FeMoS-Chalcogels.¹⁰⁻¹⁶ The details of their finding are shown in Table 1. However, compared with the photocatalytic H₂ production, N₂ photofixation is more challenging because of the hard formation of high-energy N₂ intermediates (N₂⁻ or N₂H) during the N₂ photofixation process.¹²

g-C₃N₄, which is shown to function as a semiconductor photocatalyst, has received more and more attentions. This is due to its special physicochemical properties, such as moderate band gap, unique electronic structure and special optical properties. However, as a metal-free organic semiconductor material, its photocatalytic performance is greatly limited by the fast charge recombination and insufficient absorption of visible light.¹⁷ Therefore, some g-C₃N₄ based heterostructured photocatalysts coupling with other semiconductors have been developed in recent years. Metal oxides and sulphides are widely used as this semiconductor to form the heterojunction composites with g-C₃N₄. In addition to single metal sulfide, some multi-metal sulfides coupled g-C₃N₄ composites are also reported, including ZnSnCdS/g-C₃N₄,¹⁸ ZnCdS/g-C₃N₄,¹⁹ and ZnMoCdS/g-C₃N₄.²⁰ However, few studies concerning multi-metal oxide (MMO) coupled g-C₃N₄ composites are reported.^{21,22} With the tunable composition, MMO possesses the special optical properties and electronic structure, leading to the formation of tunable band structure. This is beneficial to the energy level matching of two semiconductors, which is significant important to form the heterojunction.²³ Chen *et al.*

College of Chemistry, Chemical Engineering, and Environmental Engineering, Liaoning Shihua University, Fushun 113001, Liaoning Province, P. R. China. E-mail: hushaozhenglnpu@163.com



Table 1 The details of previous work concerning N₂ photofixation

Ref. number	Author	Year	Finding
7	Ranjit	1996	Noble-metal-loaded TiO ₂ was used as photocatalyst. A correlation between the M–H bond strength and the yield of ammonia was found
8	Rusina	2003	Fe ₂ Ti ₂ O ₇ was used as photocatalysts for N ₂ photofixation
9	Hoshino	2001	Titanium oxide (TiO _x) with a conducting polymer material (P3MeT) was used as photocatalyst
10	Dong	2015	They observed that nitrogen vacancies could endow g-C ₃ N ₄ with the photocatalytic N ₂ fixation ability
11	Zhao	2014	They used Fe-doped TiO ₂ with highly exposed (1 0 1) facets to enhance nitrogen photofixation performance
12	Zhu	2013	They demonstrated that illuminated hydrogen-terminated diamond yields facile electron emission into water, thus inducing reduction of N ₂ to NH ₃ at ambient temperature and pressure
13	Hu	2016	They found the sulfur vacancies in ternary metal sulfide plays important role on the N ₂ photofixation ability
14	Kitano	2012	They found that a Ru-loaded [Ca ₂₄ Al ₂₈ O ₆₄] ⁴⁺ (e [−]) ₄ (Ru/C12A7: e [−]), which has high electron-donating power and chemical stability, works as an efficient catalyst for ammonia synthesis
15	Banerjee	2015	They found that chalcogels containing FeMoS inorganic clusters are capable of photochemically reducing N ₂ to NH ₃
16	Li	2016	They used oxygen vacancies of BiOCl as the catalytic centers to promote the N ₂ photofixation ability

prepared ZnFe₂O₄ modified g-C₃N₄ by a simple one-pot method.²¹ As a result, the photoinduced electrons and holes in g-C₃N₄ are efficiently separated by spatial engineering of the photoactive sites, and hence enhanced photocatalytic hydrogen generation activity is obtained. Lan *et al.* synthesized Zn–In MMO/g-C₃N₄ hybrid composites by a facile thermal decomposition of Zn–In layered double hydroxide and melamine mixture precursors.²² The higher rhodamine B photocatalytic degradation rate is attributable to the unique heterostructure of the semiconductor coupling system, facilitating efficient transportation and separation of the photogenerated electron–hole pairs and thus the continuous generation of reactive oxygen species. In the best of our knowledge, no studies on the nitrogen photofixation performance over tri-component MMO/g-C₃N₄ heterojunction photocatalysts have been reported.

In this work, by tuning the metal ratio, Z-scheme g-C₃N₄/Mg_{1.1}Al_{0.3}Fe_{0.2}O_{1.7} MMO nanorods composite was prepared *in*

situ. Compared with the ectopic preparation, the heterojunction photocatalysts prepared by this method displayed stronger interaction between g-C₃N₄ and MMO. The nitrogen photofixation performance under visible light was tested to evaluate the performance of the prepared catalysts. The possible Z-scheme mechanism is proposed.

Experimental

Preparation and characterization

All the chemicals used in this experiment were reagent grade and without further treatment. Mixed salt solutions of Mg(NO₃)₂·6H₂O, Al(NO₃)₃·6H₂O and Fe(NO₃)₃·9H₂O (molar ratio Mg : Al : Fe = 10 : 3 : 2) were added into 80 mL deionized water under stirring. Then, desired amount of urea (molar ratio urea/total metal = 1.5) was added. The obtained solution was placed in a stainless autoclave, which has a 100 mL Teflon inner liner. The autoclave was sealed, placed in an oven and maintained at 120 °C for 8 h. The solid was collected by centrifugation, washed with deionized water and dried at 70 °C. The obtained solid was annealed at 520 °C for 2 h (at a rate of 5 °C min^{−1}), and denoted as MgAlFeO. 4 g of dicyandiamide was annealed at 520 °C for 2 h (at a rate of 5 °C min^{−1}). The obtained g-C₃N₄ catalyst was denoted as CN.

0.2, 0.4, 0.8 and 1.6 g of MgAlFeO was added into 20 mL of deionized water respectively and ultrasonicated for 30 min to obtain a suspension. Then, 4 g of dicyandiamide was added under stirring. The suspension was heated and maintained at 60 °C for 10 min to dissolve the dicyandiamide. The suspension was cooled down to room temperature under stirring, during which dicyandiamide was separated out and attached onto MgAlFeO surface. The solid was filtrated, dried at 80 °C and annealed at 520 °C for 2 h (at a rate of 5 °C min^{−1}). The obtained product was denoted as MgAlFeO(1)-CN, MgAlFeO(2)-CN, MgAlFeO(3)-CN and MgAlFeO(4)-CN. MgAlFeO@CN, with the same mass ratio as MgAlFeO(2)-CN, was prepared using ectopic preparation method according to previous work.²⁴ For comparison, the mechanical mixture of CN and MgAlFeO with the same mass ratio as MgAlFeO(2)-CN was also prepared. In order to investigate the reaction mechanism, MMO with other metal ratio (molar ratio Mg : Al : Fe = 1 : 1 : 1; 1 : 2 : 3 and 3 : 2 : 1) were prepared and denoted as MAFO, MA₂F₃O and M₃A₂FO. The obtained MMO were also used to synthesize heterojunction catalysts following the same procedure as in the synthesis of MgAlFeO(2)-CN. The products were denoted as MAFO-CN, MA₂F₃O-CN and M₃A₂FO-CN.

The XRD patterns of the prepared samples were recorded on a Rigaku D/max-2400 instrument using Cu-Kα radiation (λ = 1.54 Å). The scan rate, step size, voltage and current were 0.05° min^{−1}, 0.01°, 40 kV and 30 mA, respectively. UV-vis spectroscopy was carried out on a JASCO V-550 model UV-vis spectrophotometer using BaSO₄ as the reflectance sample. The morphologies of prepared catalyst were observed by using a scanning electron microscope (SEM, JSM 5600LV, JEOL Ltd.). Nitrogen adsorption was measured at −196 °C on a Micromeritics 2010 analyser. All the samples were degassed at 393 K prior to the measurement. The BET surface area (*S*_{BET}) was



calculated based on the adsorption isotherm. ICP was performed on a Perkin-Elmer Optima 3300DV apparatus. The XPS measurements were performed on a Thermo Escalab 250 XPS system with Al K α radiation as the excitation source. The binding energies were calibrated by referencing the C 1s peak (284.6 eV) to reduce the sample charge effect. The photoluminescence (PL) spectra were measured at room temperature with a fluorospectrophotometer (FP-6300) using a Xe lamp as the excitation source. Electrochemical impedance spectra (EIS) made from these as-made materials were measured *via* an EIS spectrometer (EC-Lab SP-150, BioLogic Science Instruments) in a three-electrode cell by applying 10 mV alternative signal *versus* the reference electrode (SCE) over the frequency range of 1 MHz to 100 mHz. The cyclic voltammograms were measured in 0.1 M KCl solution containing 2.5 mM K₃[Fe(CN)₆]/K₄[Fe(CN)₆] (1 : 1) as a redox probe with the scanning rate of 20 mV s^{−1} in the same three electrode cell as EIS measurement.

Isotopic labeling experiments are carried out as follow. Ar was used to eliminate air and the possible adsorbed ammonia in the reaction system. ¹⁵N₂ was passed through the reaction mixture for 30 min. After that, the reactor was sealed. Other experiment conditions were the same as those for ¹⁴N₂ photo-fixation. The produced ¹⁵NH₄⁺ reacts with phenolic and hypochlorite to form ¹⁵N labeled indophenol, which was analyzed by LC-MS. The sample for LC-MS analysis was prepared as follows. 0.5 mL of the reaction reacted with 0.1 mL of 1% phenolic solution in 95% ethanol. Then, 0.375 mL of 1% NaClO solution and 0.5 mL of 0.5% sodium nitroprusside solution were added into above solution. MS studies were carried on an Ultimate 3000-TSQ (LCMS-ESI).

Photocatalytic reaction

The nitrogen photofixation property was evaluated according to previous literature.¹¹ The nitrogen photofixation experiments were performed in a double-walled quartz reactor in air. For these experiments, 0.2 g of photocatalyst was added to a 500 mL 0.789 g L^{−1} ethanol as a hole scavenger.¹¹ The suspension was dispersed using an ultrasonicator for 10 min. During the photoreaction under visible light irradiation, the suspension was exposed to a 250 W high-pressure sodium lamp with main emission in the range of 400 to 800 nm, and N₂ was bubbled at 100 mL min^{−1} through the solution. The UV light portion of the sodium lamp was filtered by a 0.5 M NaNO₂ solution. All runs were conducted at ambient pressure and 30 °C. At given time intervals, 5 mL aliquots of the suspension were collected and immediately centrifuged to separate the liquid samples from the solid catalyst. The concentration of ammonia was measured using the Nessler's reagent spectrophotometry method (JB7478-87) with a UV-2450 spectrophotometer (Shimadzu, Japan).^{11,25}

Results and discussion

The XRD patterns of as-prepared catalysts are shown in Fig. 1a. Two typical diffraction peaks of g-C₃N₄ are present in the CN. The peak at 13.1° corresponds to in-plane structural packing motif of tri-s-triazine units, which is indexed as (100) peak. The

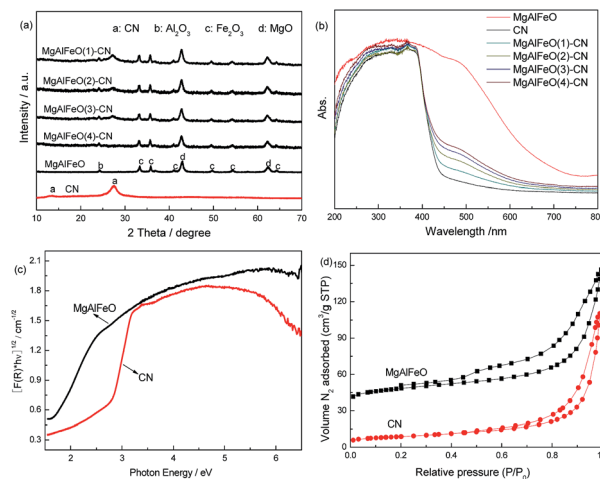


Fig. 1 XRD patterns (a) UV-vis spectra (b), plots of the transformed Kubelka–Munk function *versus* the energy of light (c) and N₂ adsorption–desorption isotherms (d) of as-prepared catalysts.

peak at 27.5° corresponds to interlayer stacking of aromatic segments with distance of 0.324 nm, which is indexed as (002) peak. For MgAlFeO, nine diffraction peaks are observed, which are assigned to MgO, Al₂O₃ and Fe₂O₃, respectively.^{26–28} It is noted that no characteristic diffractions related to g-C₃N₄ are observed in the MgAlFeO(4)-CN, probably due to the low g-C₃N₄ content. With the increased CN content, the characteristic diffractions of g-C₃N₄ can be found clearly. No diffraction peak shift is observed indicating that no metal doping occurs. The UV-vis spectra of the as-prepared heterojunction photocatalysts, as well as those of CN and MgAlFeO, are shown in Fig. 1b. The band gaps are estimated from the tangent lines in the plots of the square root of the Kubelka–Munk function as a function of the photon energy (Fig. 1c).²⁹ CN displays an absorption edge at approximately 452 nm, corresponding to a band gap of 2.74 eV (Table 2). The absorption edge for MgAlFeO is observed at 705 nm, and the corresponding band gap is estimated to be 1.76 eV. For the as-prepared heterojunction photocatalysts, the typical two absorption edges for CN and MgAlFeO are observed, hinting the heterojunction photocatalysts are composed of these two components. The higher MgAlFeO content, the stronger visible light absorption for these heterojunction photocatalysts, corresponding to the color change from light yellow to saffron yellow.

To characterize the specific surface area of as-prepared catalysts, the nitrogen adsorption and desorption isotherms were measured (Fig. 1d). The isotherm of CN and MgAlFeO are of classical type IV, suggesting the presence of mesopores. The

Table 2 The band position and band gap energy of as-prepared catalysts

Sample	CN	MgAlFeO	MAFO	MA ₂ F ₃ O	M ₃ A ₂ FO
CB position (V)	−1.53	0.11	−0.52	−0.59	−0.67
VB position (V)	+1.21	+1.65	+1.46	+1.34	+1.21
Band gap (eV)	2.74	1.76	1.98	1.93	1.88



BET specific surface areas (S_{BET}) of CN, MgAlFeO(1)-CN, MgAlFeO(2)-CN, MgAlFeO(3)-CN, MgAlFeO(4)-CN and MgAlFeO are calculated to be 10.5, 12.6, 20.7, 28.9 and 38.6 $\text{m}^2 \text{g}^{-1}$. The large S_{BET} can promote adsorption, desorption and diffusion of reactants and products, which is favorable to the photocatalytic performance. Table 3 shows the components of as-prepared catalysts obtained by ICP. The C and N contents for CN are 39 wt% and 57 wt%, which is close to the theoretical values. For MgAlFeO, the Mg, Al, Fe and O contents are 33 wt%, 11.5 wt%, 15.5 wt% and 40 wt%, respectively. Thus the actual atomic ratio is $\text{Mg}_{1.1}\text{Al}_{0.3}\text{Fe}_{0.2}\text{O}_{1.7}$. For the as-prepared heterojunction photocatalysts, the MgAlFeO content is 11.7 wt%, 23.6 wt%, 59.3 wt%, and 79.7 wt% for MgAlFeO(1)-CN, MgAlFeO(2)-CN, MgAlFeO(3)-CN and MgAlFeO(4)-CN, respectively.

The morphologies of the representative samples were examined using SEM analysis (Fig. 2). Fig. 2a shows that as-prepared CN possesses smooth layer structure. MgAlFeO has a spherical structure assembled by dozens of nanorods (Fig. 2b). In the case of as-prepared heterojunction catalysts, spherical structure MgAlFeO can not be observed. The MgAlFeO nanorods attach on the CN surface to assemble CN/MgAlFeO nanocomposites (Fig. 2c and d). However, some obvious differences between MgAlFeO(2)-CN and MgAlFeO@CN can be observed. For MgAlFeO@CN (Fig. 2c) MgAlFeO nanorods stick to the CN surface. The interaction between MgAlFeO and CN is poor. In the case of MgAlFeO(2)-CN (Fig. 2d), the MgAlFeO nanorods seem to embed into the CN surface. Thus it is deduced that the interaction between MgAlFeO and CN should be stronger than that of MgAlFeO@CN. This stronger interaction can result in the higher interfacial charge transfer rate and more stable CN/MgAlFeO composite structure.

The structure of the as-prepared heterojunction catalyst is investigated by XP spectra. In Mg 2p, Al 2p and Fe 2p regions (Fig. 3a–c), the binding energies for MgAlFeO located at 49.7, 73.8 and 711.3 eV are assigned to the Mg^{2+} , Al^{3+} and Fe^{3+} respectively.^{30–32} For MgAlFeO(2)-CN, the binding energies in Mg 2p, Al 2p and Fe 2p regions exhibit blue-shifts compared with that of MgAlFeO. This electron density change is probably due to the electron transfer from electron-rich g- C_3N_4 to MgAlFeO. In O 1s region (Fig. 3d), the MgAlFeO displays a single peak at 531.6 eV, which is assigned to the O^{2-} bond to the metal ions. For MgAlFeO(2)-CN, besides this M (metal)–O bond, another peak at 533 eV is observed. As reported by previous literatures, this peak should be assigned to the adsorbed oxygen species.^{33–35}

In Fig. 3e, the spectra of CN and MgAlFeO(2)-CN in the C 1s region can be fitted with three contributions located at 284.6, 285.8 and 287.8 eV. They are attributed to the C–C bond, which

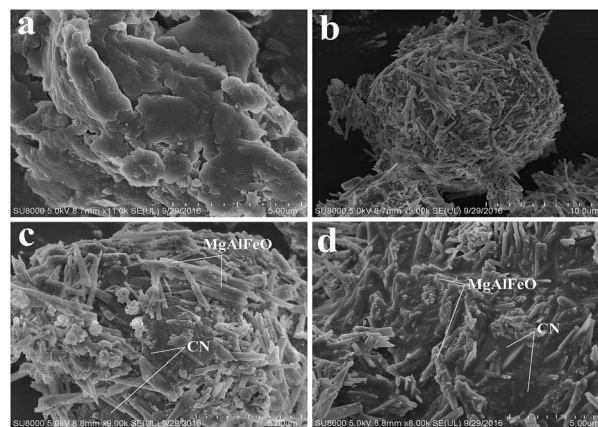


Fig. 2 SEM images of CN (a), MgAlFeO (b), MgAlFeO@CN (c) and MgAlFeO(2)-CN (d).

originated from sp^2 C atoms bonded to N in an aromatic ring ($\text{N}-\text{C}=\text{N}$); $\text{C}=\text{N}$ or $\text{C}\equiv\text{N}$, which could be attributed to defect-containing sp^2 -hybridized carbon atoms present in graphitic domains; and pure graphitic sites in a CN matrix.³⁶ In Fig. 3f, the main N 1s peak of CN located at 398.5 eV can be assigned to sp^2 -hybridized nitrogen ($\text{C}=\text{N}-\text{C}$), thus confirming the presence of sp^2 -bonded graphitic carbon nitride. The peak at a higher binding energy of 400.4 eV is attributed to tertiary nitrogen ($\text{N}-(\text{C})_3$) groups.³⁷ For MgAlFeO(2)-CN, the remarkable shift to higher binding energy is observed, indicating the decreased electron density of nitrogen atoms. Combined with

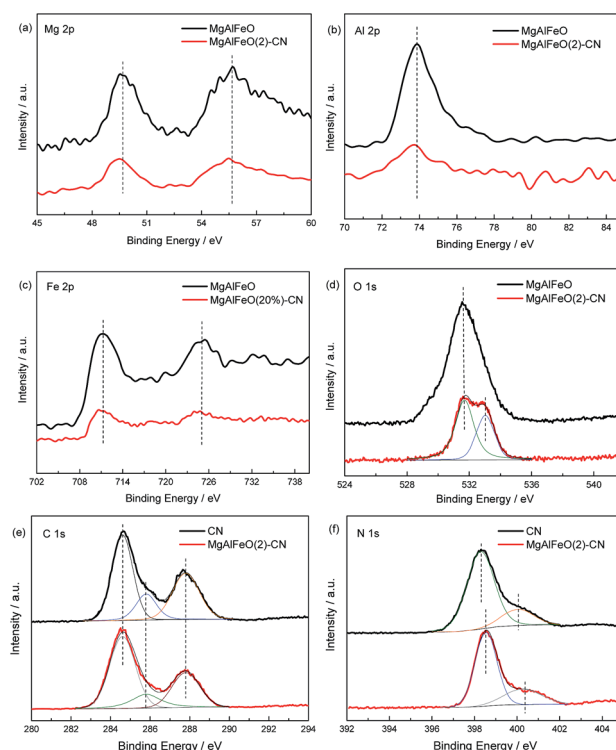


Fig. 3 XPS of as prepared catalysts in the region of Mg 2p (a), Al 2p (b), Fe 2p (c), O 1s (d), C 1s (e) and N 1s (f).

Table 3 The components of as-prepared catalysts obtained by ICP

Sample	C/wt%	N/wt%	Mg/wt%	Al/wt%	Fe/wt%	O/wt%
CN	39	57	—	—	—	4
MgAlFeO	—	—	34	11.5	15	39.5
MgAlFeO(1)-CN	35.1	53.2	3.6	1.4	1.8	4.9
MgAlFeO(2)-CN	30.6	46.8	7.0	2.6	3.4	9.6
MgAlFeO(3)-CN	15.5	25.2	19.6	6.5	9.2	24
MgAlFeO(4)-CN	7.9	12.4	26.3	8.5	12.3	32.6



the phenomenon of binding energy shift in Mg 2p, Al 2p and Fe 2p regions, it is deduced that the strong electronic interaction between the CN and MgAlFeO is formed in MgAlFeO(2)-CN. Besides, no new binding energy is observed for MgAlFeO(2)-CN, indicating that the interaction between CN and MgAlFeO is not chemical bond.

The energy level position of as-prepared catalyst is confirmed by VB XPS. In Fig. 4a, the VB positions of CN and MgAlFeO are +1.21 and +1.65 V (Table 2). It is obtained from the UV-vis results that the band gaps for CN and MgAlFeO are 2.74 and 1.76 eV. Thus the E_{CB} for CN and MgAlFeO is -1.53 and -0.11 V, respectively. Fig. 4b shows the UV-vis spectra of MAFO, MA_2F_3O and M_3A_2FO . The absorption edges for MAFO, MA_2F_3O and M_3A_2FO are 626, 644 and 659 nm, and the corresponding band gaps are estimated to be 1.98, 1.93 and 1.88 eV, respectively. In Fig. 4c, the VB positions of MAFO, MA_2F_3O and M_3A_2FO are +1.46, +1.34 and +1.21 V. Combine with the UV-vis result, the E_{CB} for MAFO, MA_2F_3O and M_3A_2FO are -0.52 , -0.59 and -0.67 V, respectively. These results indicate that the component of MMO strongly influences the optical property and energy level position of as-prepared materials.

The FT-IR result is provided in Fig. 5. For CN, a series of peaks in the range from 1200 to 1600 cm^{-1} are attributed to the typical stretching modes of CN heterocycles, while the sharp peak located at 810 cm^{-1} is assigned to the bending vibration of heptazine rings, which indicating the synthesized g- C_3N_4 is composed of heptazine units. The broad absorption band around 3200 cm^{-1} is originated from the stretching vibration of N-H bond, associated with uncondensed amino groups. In the case of MgAlFeO, the peak located at 446 and 480 cm^{-1} are assigned to the Fe-O stretching and bending vibration modes.³⁸ The peaks at 674 and 1533 cm^{-1} are attributed to the Mg-O bond.³⁹ The peaks located at 882, 982 and 1372 cm^{-1} are assigned to the Al-O bond.⁴⁰ In the case of MgAlFeO(2)-CN, no peak for metal oxide is observed. Theerthagiri *et al.* prepared α - $Fe_2O_3/g-C_3N_4$ nanocomposites and found the similar phenomenon.³⁸ Besides, no new peak is observed for MgAlFeO(2)-CN,

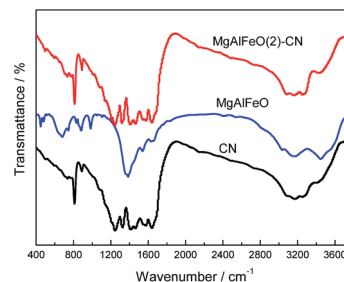


Fig. 5 FT-IR result of as-prepared catalysts.

indicating no chemical bond is formed between two components. XPS result confirms this point of view.

EIS and PL spectra were used to characterize charge-carrier migration and confirm the interfacial charge transfer effect of the as-prepared heterojunction catalysts. As shown in Fig. 6a, after coupling with MgAlFeO, the as-prepared heterojunction catalysts exhibit a decreased arc radius compared to that of CN. In general, the radius of the arc in the EIS spectra reflects the reaction rate on the surface of the electrode.⁴¹ The reduced arc radius indicates a diminished resistance of the working electrodes, suggesting a decrease in the solid-state interface layer resistance and the charge transfer resistance across the solid-liquid junction on the surface between CN and MgAlFeO.^{42,43} MgAlFeO(2)-CN shows the smallest arc radius, indicating that a more effective separation of photogenerated electron-hole pairs and a faster interfacial charge transfer occur. This is reasonable because, with this CN/MgAlFeO mass ratio, CN and MgAlFeO have the approximate S_{BET} (10.5 and 38.6 $m^2 g^{-1}$ for CN and MgAlFeO, Fig. 1d). They can contact with each other as much as possible, leading to the formation of the maximum area of the heterojunction. In Fig. 6b, the PL intensity follows the sequence MgAlFeO(2)-CN < MgAlFeO(1)-CN < MgAlFeO(3)-CN < MgAlFeO(4)-CN < CN. In general, at a lower PL intensity, the separation rate of the photogenerated electron-hole pairs is higher. This confirms the efficient transfer of photoinduced electrons and holes between CN and MgAlFeO in heterojunction catalysts. In addition, both EIS and PL spectra show that the interfacial charge transfer efficiency of MgAlFeO@CN is much lower than that of MgAlFeO(2)-CN. This confirms the stronger interaction between MgAlFeO and CN in MgAlFeO(2)-CN.

Fig. 7a shows the NH_4^+ generation rate ($r(NH_4^+)$) over the as-prepared catalysts under visible light. The control experiment results indicate that the $r(NH_4^+)$ can be ignored in the absence

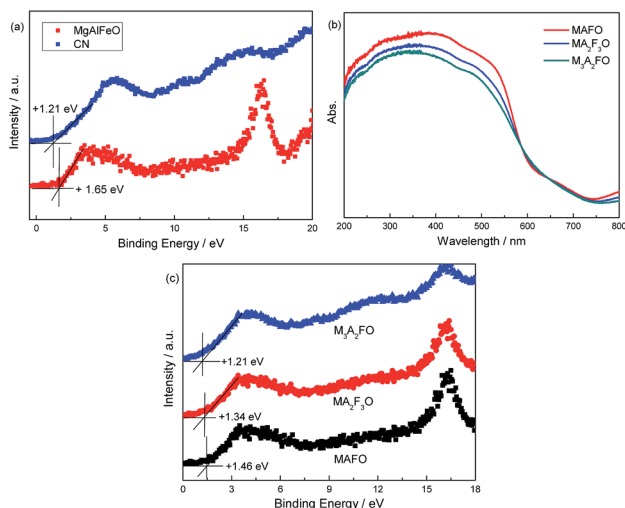


Fig. 4 VB XPS of MgAlFeO and CN (a), UV-vis (b) and VB XPS (c) of MAFO, MA_2F_3O and M_3A_2FO .

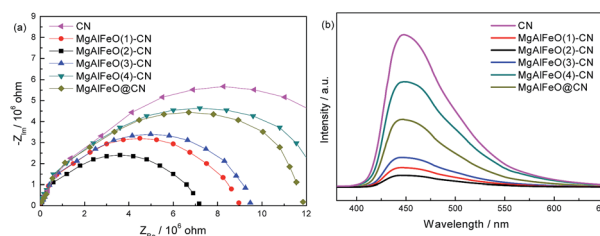


Fig. 6 EIS (a) and PL (b) results of as-prepared catalysts.



of irradiation, N_2 or photocatalyst, indicating that nitrogen photofixation occurs *via* a photocatalytic process. Interestingly, $MgAlFeO$ shows almost no activity though it can absorb visible light, indicating it is not the active component in this reaction system. CN shows the $r(NH_4^+)$ of $2.1 \text{ mg L}^{-1} \text{ h}^{-1} \text{ g}_{\text{cat}}^{-1}$. The $r(NH_4^+)$ for as-prepared heterojunction photocatalyst obviously improves compared with CN. $MgAlFeO(2)\text{-CN}$ displays the highest $r(NH_4^+)$, $7.5 \text{ mg L}^{-1} \text{ h}^{-1} \text{ g}_{\text{cat}}^{-1}$, which is approximately 3.5-fold higher than that of CN. $AgNO_3$, as electron scavenger, obviously decreases the nitrogen photofixation ability of $MgAlFeO(2)\text{-CN}$, as shown in Fig. 7b. This hints that the main active species of this nitrogen photofixation reaction is photo-generated electron. The $r(NH_4^+)$ can be ignorant when using DMF and DMSO as aprotic solvents instead of water (Fig. 7b). This confirms that H_2O as the proton source is necessary for the nitrogen photofixation process. In order to further investigate the nitrogen source of NH_4^+ , the N_2 photofixation ability of $MgAlFeO(2)\text{-CN}$ under ^{15}N isotope-labeled N_2 (purity > 98%) was performed. A strong ^{15}N labeled indophenol anion mass spectroscopy signal presents at 199 m/z in LC-MS studies (Fig. 7c). The intensity of this signal is obviously higher than the ^{14}N : ^{15}N natural abundance ratio, confirming that N_2 is the nitrogen source of generated NH_4^+ in this N_2 photofixation process. Fig. 7d compares the photocatalytic N_2 fixation stability of as-prepared catalysts. The mixture of $MgAlFeO$ and CN exhibits much lower $r(NH_4^+)$ than that of $MgAlFeO(2)\text{-CN}$ and $MgAlFeO@CN$ which confirms the interfacial charge transfer plays an important role on the photocatalytic performance. $MgAlFeO@CN$ shows the $r(NH_4^+)$ of $4.2 \text{ mg L}^{-1} \text{ h}^{-1} \text{ g}_{\text{cat}}^{-1}$, lower than that of $MgAlFeO(2)\text{-CN}$. Besides that, $MgAlFeO@CN$ displays a gradually decreased activity, which is approximately equal to that of mechanical mixture after 20 h reaction. This should be due to the weaker interaction between CN and $MgAlFeO$ for $MgAlFeO@CN$ compared with $MgAlFeO(2)\text{-CN}$. The week interaction not only results in the low interfacial charge transfer rate but also causes the composite split to the mixture of CN

and $MgAlFeO$ during the reaction, leading to the poor stability. In the contrary, $MgAlFeO(2)\text{-CN}$ shows the stable N_2 photofixation ability. The strong interaction causes the stable CN/ $MgAlFeO$ composite structure, thus leads to this stable activity. The actual atomic ratio of $MgAlFeO$ is $Mg_{1.1}Al_{0.3}Fe_{0.2}O_{1.7}$ obtained by ICP. According to the molar ratio, the number of oxygen atoms should be 1.85, indicating the oxygen vacancy should exist. It is also reported by Li *et al.* that the introduction of oxygen vacancies could activate N_2 and promote interfacial electron transfer.²⁵ However, the $MgAlFeO$ shows very poor N_2 photofixation ability, probably due to the poor CB driving force. For the as-prepared heterojunction photocatalysts, the actual atomic ratio of multi-metal oxide is hardly obtained because the oxygen also exists in $g\text{-C}_3N_4$. In order to investigate the influence of oxygen vacancy on the N_2 photofixation ability, the $MgAlFeO(2)\text{-CN}$ was calcined at 520°C in O_2 atmosphere for 4 h to eliminate the oxygen vacancy. The obtained catalyst shows the similar N_2 photofixation ability ($7.3 \text{ mg L}^{-1} \text{ h}^{-1} \text{ g}_{\text{cat}}^{-1}$) to that of $MgAlFeO(2)\text{-CN}$ ($7.5 \text{ mg L}^{-1} \text{ h}^{-1} \text{ g}_{\text{cat}}^{-1}$). Thus it is deduced that the oxygen vacancy should be not responsible for the improved N_2 photofixation ability of heterojunction photocatalyst.

It is reported that the standard redox potential for N_2/NH_3 is -0.09 V against NHE.⁹ The reduction potential of CB electrons in CN is more negative than the redox potential for N_2/NH_3 . Thus the CB electrons of CN can reduce the N_2 molecule and form the NH_3 theoretically. However, $MgAlFeO$ shows almost no N_2 photofixation activity though it can absorb visible light. This is probably due to the E_{CB} of $MgAlFeO$ is close to the standard redox potential for N_2/NH_3 , leading to the poor CB driving force. This CB driving force determines the migration rate of photo-generated holes and electrons, causing the ignorant N_2 photofixation ability.⁴⁴ Fig. 8a shows the TOC removal rate of atrazine (a powerful herbicides) in the presence of N_2 over as-prepared catalysts. In the contrary of N_2 photofixation ability, the TOC removal rate for $MgAlFeO$ is 28%, whereas CN shows almost no activity. The redox potentials for $^{\bullet}OH/OH^-$ is $+1.99 \text{ V}$.⁴⁵ The VB

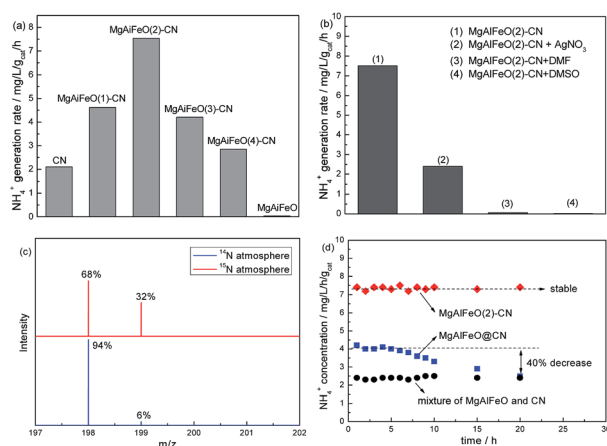


Fig. 7 The NH_4^+ production ability over as-prepared catalysts (a), NH_4^+ production ability of $Fe_{0.05}\text{-CN}$ using $AgNO_3$ as the electron scavenger and in aprotic solvents DMF and DMSO (b), the mass spectra of the indophenol prepared from different atmosphere (c) and photocatalytic N_2 fixation stability of as-prepared catalysts (d).

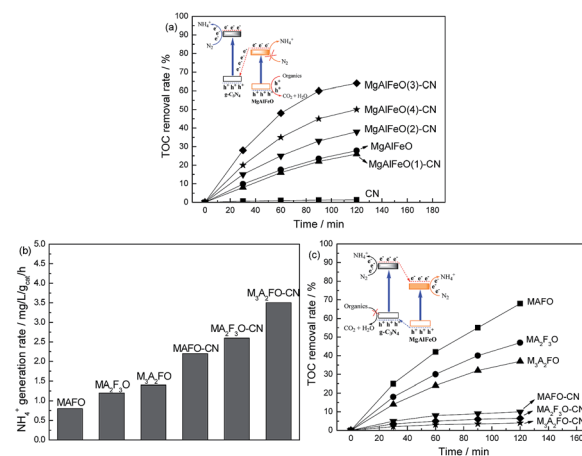


Fig. 8 The TOC removal rate of atrazine in the presence of N_2 over as-prepared catalysts (a), N_2 photofixation ability (b) and TOC removal rate of atrazine in the presence of N_2 (c) over MAFO, MA_2F_3O , MA_3A_2FO , $MAFO\text{-CN}$, $MA_2F_3O\text{-CN}$ and $MA_3A_2FO\text{-CN}$.

holes in CN and MgAlFeO are not positive enough to generate $\cdot\text{OH}$. Thus the main active species should be holes for the atrazine photodegradation. The obvious activity difference in atrazine photodegradation between CN and MgAlFeO indicates that the VB holes in CN is not positive enough to oxidize atrazine but the VB holes in MgAlFeO can. For the as-prepared heterojunction photocatalysts, the TOC removal rates improve obviously. This hints that, in the as-prepared heterojunction photocatalysts, the photogenerated holes are in the VB of MgAlFeO but not CN. The transfer route of electrons and holes for heterojunction photocatalysts is shown in Fig. 8a inset. Because of the poor CB driving force, the photogenerated electrons in the CB of MgAlFeO can not react with N_2 molecule to form NH_4^+ . Consequently, these electrons tend to transfer to the VB of CN and recombine with the photogenerated holes there, leaving photogenerated holes in the VB of MgAlFeO to oxidize atrazine.

Fig. 8b shows the N_2 photofixation ability over MAFO, $\text{MA}_2\text{F}_3\text{O}$, $\text{M}_3\text{A}_2\text{FO}$, MAFO-CN, $\text{MA}_2\text{F}_3\text{O}$ -CN and $\text{M}_3\text{A}_2\text{FO}$ -CN. MAFO, $\text{MA}_2\text{F}_3\text{O}$ and $\text{M}_3\text{A}_2\text{FO}$ exhibit much higher N_2 photofixation ability than that of MgAlFeO ($0.2 \text{ mg L}^{-1} \text{ h}^{-1} \text{ g}_{\text{cat}}^{-1}$), which should be due to that the proper energy level position results in the powerful CB driving force. However, the $r(\text{NH}_4^+)$ for MAFO-CN, $\text{MA}_2\text{F}_3\text{O}$ -CN and $\text{M}_3\text{A}_2\text{FO}$ -CN are much lower than that of MgAlFeO(2)-CN ($7.5 \text{ mg L}^{-1} \text{ h}^{-1} \text{ g}_{\text{cat}}^{-1}$). This hints that their transfer routes of electrons and holes are probably different from each other. In order to confirm this point of view, the TOC removal rates of atrazine in the presence of N_2 over MAFO, $\text{MA}_2\text{F}_3\text{O}$, $\text{M}_3\text{A}_2\text{FO}$, MAFO-CN, $\text{MA}_2\text{F}_3\text{O}$ -CN and $\text{M}_3\text{A}_2\text{FO}$ -CN are measured (Fig. 8c). Interestingly, the MAFO-CN, $\text{MA}_2\text{F}_3\text{O}$ -CN and $\text{M}_3\text{A}_2\text{FO}$ -CN show much lower TOC removal rate than that of MAFO, $\text{MA}_2\text{F}_3\text{O}$ and $\text{M}_3\text{A}_2\text{FO}$, indicating that the photogenerated holes are in the VB of CN but not MgAlFeO in these heterojunction photocatalysts, as shown in Fig. 8c inset.

According to the results mentioned above, the possible “Z-scheme” mechanism over MgAlFeO(2)-CN is proposed, as shown in Fig. 9. Upon visible-light irradiation, the photogenerated electrons and holes are formed in both CN and MgAlFeO. The electrons in CB of CN react with N_2 to form NH_4^+ . Whereas, the N_2 photofixation can not be occurred in CB of MgAlFeO because of the poor CB driving force. Consequently, the photogenerated electrons in the CB of MgAlFeO tend to transfer to the VB of CN and recombine with the photogenerated holes there. Therefore,

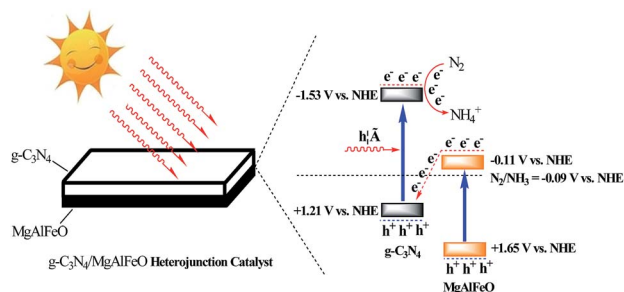


Fig. 9 The possible Z-scheme mechanism over MgAlFeO(2)-CN.

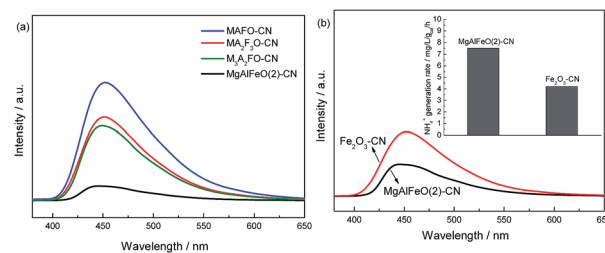


Fig. 10 PL spectra of MgAlFeO(2)-CN, MAFO-CN, $\text{MA}_2\text{F}_3\text{O}$ -CN and $\text{M}_3\text{A}_2\text{FO}$ -CN (a) and the comparison of PL and N_2 photofixation ability of MgAlFeO(2)-CN and Fe_2O_3 -CN (b).

the photogenerated electrons in CB of CN can not back to VB to recombine with the photogenerated holes but react with N_2 molecule, leading to the promoted N_2 photofixation ability. In the case of MAFO-CN, $\text{MA}_2\text{F}_3\text{O}$ -CN and $\text{M}_3\text{A}_2\text{FO}$ -CN system, because of the proper energy level position of MMO, the photogenerated electrons in the CB of MMO can react with N_2 molecule but not transfer to VB of CN to recombine with the photogenerated holes there. Thus the “Z-scheme” electrons transfer route is not formed, leading to the lower separation rate and N_2 photofixation ability than that of MgAlFeO(2)-CN.

In order to confirm the different electrons transfer route among them, the PL spectra of MgAlFeO(2)-CN, MAFO-CN, $\text{MA}_2\text{F}_3\text{O}$ -CN and $\text{M}_3\text{A}_2\text{FO}$ -CN are compared with each other (Fig. 10a). Obviously, the MAFO-CN, $\text{MA}_2\text{F}_3\text{O}$ -CN and $\text{M}_3\text{A}_2\text{FO}$ -CN show the comparable PL intensities, which are much higher than that of MgAlFeO(2)-CN. This hints that the interfacial charge transfer efficiency of MgAlFeO(2)-CN is much higher than that of MAFO-CN, $\text{MA}_2\text{F}_3\text{O}$ -CN and $\text{M}_3\text{A}_2\text{FO}$ -CN, confirming the “Z-scheme” mechanism over MgAlFeO(2)-CN. In addition, since MgO and Al_2O_3 are non-conductive, the semi-conductivity of the mixed oxides should come from Fe_2O_3 . It is known that the coupling of Fe_2O_3 with $\text{g-C}_3\text{N}_4$ can obviously improve the photocatalytic performance.^{46–49} Thus the Fe_2O_3 -CN with the same mass ratio with MgAlFeO(2)-CN is prepared for comparison. The PL spectra and N_2 photofixation performance of Fe_2O_3 -CN are investigated (Fig. 10b). Obviously, the PL intensity of Fe_2O_3 -CN is much higher than that of MgAlFeO(2)-CN, hinting its lower interfacial charge transfer efficiency. It is known that the E_{CB} and E_{VB} of Fe_2O_3 are +0.49 and +2.29 eV, respectively.³⁸ Thus the band gap energy and band position of Fe_2O_3 are obviously different from that of as-prepared MgAlFeO. The E_{CB} of Fe_2O_3 is much positive than that of MgAlFeO (−0.11 eV), causing the lower driving force from E_{CB} of Fe_2O_3 to E_{VB} of $\text{g-C}_3\text{N}_4$ than that of MgAlFeO(2)-CN. Thus the interfacial charge transfer efficiency and N_2 photofixation performance of Fe_2O_3 -CN are lower than that of MgAlFeO(2)-CN.

Conclusions

In this work, Z-scheme $\text{g-C}_3\text{N}_4/\text{MgAlFeO}$ nanorods composite was prepared *in situ* by tuning the metal ratio. SEM results show that the MgAlFeO nanorods stick but not attach to the CN surface, leading to the strong electronic coupling exists between two components. This strong electronic coupling results in



more effective separation of photogenerated electron–hole pairs and faster interfacial charge transfer, causing the higher activity and stability of N₂ photofixation. Because of the poor CB driving force, MgAlFeO shows almost no N₂ photofixation ability. Thus, the photogenerated electrons can not be consumed in the CB of MgAlFeO. Consequently, these photogenerated electrons tend to transfer to the VB of CN and recombine with the photo-generated holes there, forming the “Z-scheme” interfacial charge transfer mechanism. With the MgAlFeO mass percentage of 23.6%, MgAlFeO(2)-CN exhibits the highest NH₄⁺ generation rate under visible light (7.5 mg L^{−1} h^{−1} g_{cat}^{−1}), which is 3.5-fold greater than that of individual CN.

Acknowledgements

This work was supported by the Natural Science Foundation of Liaoning Province (2015020590) and Pilot Program of University of Liaoning Innovation and Education Reform.

Notes and references

- 1 M. E. Vol'pin, V. B. Shur and E. G. Berkovich, *Inorg. Chim. Acta*, 1998, **280**, 264–274.
- 2 G. J. Leigh, *Science*, 1998, **279**, 506–507.
- 3 E. E. van Tamelen and B. Akermark, *J. Am. Chem. Soc.*, 1968, **90**, 4492–4493.
- 4 C. R. Dickson and A. J. Nozik, *J. Am. Chem. Soc.*, 1978, **100**, 8007–8009.
- 5 G. N. Schrauzer and T. D. Guth, *J. Am. Chem. Soc.*, 1977, **99**, 7189–7193.
- 6 K. T. Ranjit and B. Viswanathan, *Indian J. Chem., Sect. A: Inorg., Bio-inorg., Phys., Theor. Anal. Chem.*, 1996, **35**, 443–448.
- 7 K. T. Ranjit, T. K. Varadarajan and B. Viswanathan, *J. Photochem. Photobiol., A*, 1996, **96**, 181–185.
- 8 O. Rusina, O. Linnik, A. Eremenko and H. Kisch, *Chem.–Eur. J.*, 2003, **9**, 561–565.
- 9 K. Hoshino, *Chem.–Eur. J.*, 2001, **7**, 2727–2731.
- 10 G. H. Dong, W. K. Ho and C. Y. Wang, *J. Mater. Chem. A*, 2015, **3**, 23435–23441.
- 11 W. R. Zhao, J. Zhang, X. Zhu, M. Zhang, J. Tang, M. Tan and Y. Wang, *Appl. Catal., B*, 2014, **144**, 468–477.
- 12 D. Zhu, L. Zhang, R. E. Ruther and R. J. Hamers, *Nat. Mater.*, 2013, **12**, 836–841.
- 13 S. Z. Hu, X. Chen, Q. Li, Y. F. Zhao and W. Mao, *Catal. Sci. Technol.*, 2016, **6**, 5884–5890.
- 14 M. Kitano, Y. Inoue, Y. Yamazaki, F. Hayashi, S. Kanbara, S. Matsuishi, T. Yokoyama, S. W. Kim, M. Hara and H. Hosono, *Nat. Chem.*, 2012, **4**, 934–940.
- 15 A. Banerjee, B. D. Yuhas, E. A. Margulies, Y. B. Zhang, Y. Shim, M. R. Wasielewski and M. G. Kanatzidis, *J. Am. Chem. Soc.*, 2015, **137**, 2030–2034.
- 16 H. Li, J. Shang, J. G. Shi, K. Zhao and L. Z. Zhang, *Nanoscale*, 2016, **8**, 1986–1993.
- 17 Z. H. Chen, P. Sun, B. Fan, Q. Liu, Z. G. Zhang and X. M. Fang, *Appl. Catal., B*, 2015, **10–16**, 170–171.
- 18 S. Z. Hu, Y. M. Li, F. Y. Li, Z. P. Fan, H. F. Ma, W. Li and X. X. Kang, *ACS Sustainable Chem. Eng.*, 2016, **4**, 2269–2278.
- 19 Q. Nie, Q. Yuan and Q. Wang, *J. Mater. Sci.*, 2004, **39**, 5611–5612.
- 20 X. L. Fu, X. X. Wang, Z. X. Chen, Z. Z. Zhang, Z. H. Li, D. Y. C. Leung, L. Wu and X. Z. Fu, *Appl. Catal., B*, 2010, **95**, 393–399.
- 21 J. Chen, S. H. Shen, P. H. Guo, P. Wu and L. J. Guo, *J. Mater. Chem. A*, 2014, **2**, 4605–4612.
- 22 M. Lan, G. L. Fan, L. Yang and F. Li, *RSC Adv.*, 2015, **5**, 5725–5734.
- 23 S. Z. Hu, F. Y. Li, Z. P. Fan, F. Wang, Y. F. Zhao and Z. B. Lv, *Dalton Trans.*, 2015, **44**, 1084.
- 24 S. Nayak, L. Mohapatra and K. Parida, *J. Mater. Chem. A*, 2015, **3**, 18622–18635.
- 25 H. Li, J. Shang, Z. H. Ai and L. Z. Zhang, *J. Am. Chem. Soc.*, 2015, **137**, 6393–6399.
- 26 J. Choi, S. H. Zhang and J. M. Hill, *Catal. Sci. Technol.*, 2012, **2**, 179–186.
- 27 Y. D. Ding, G. Song, X. Zhu, R. Chen and Q. Liao, *RSC Adv.*, 2015, **5**, 30929–30935.
- 28 Z. H. Gu, K. Z. Li, S. Qing, X. Zhu, Y. G. Wei, Y. T. Li and H. Wang, *RSC Adv.*, 2014, **4**, 47191–47199.
- 29 Y. I. Kim, S. J. Atherton, E. S. Brigham and T. E. Mallouk, *J. Phys. Chem.*, 1993, **97**, 11802–11810.
- 30 H. P. R. Kannapu, C. K. P. Neeli, K. S. R. Rao, V. N. Kalevaru, A. Martin and D. R. Burri, *Catal. Sci. Technol.*, 2016, **6**, 5494–5503.
- 31 S. W. Lee, J. Heo and R. G. Gordon, *Nanoscale*, 2013, **5**, 8940–8944.
- 32 X. S. Zhou, B. Jin, R. Q. Chen, F. Peng and Y. P. Fang, *Mater. Res. Bull.*, 2013, **48**, 1447–1452.
- 33 H. Xu, J. Yan, X. J. She, L. Xu, J. X. Xia, Y. G. Xu, Y. H. Song, L. Y. Huang and H. M. Li, *Nanoscale*, 2014, **6**, 1406–1415.
- 34 K. X. Li, L. S. Yan, Z. X. Zeng, S. L. Luo, X. B. Luo, X. M. Liu, H. Q. Guo and Y. H. Guo, *Appl. Catal., B*, 2014, **156–157**, 141–152.
- 35 P. Niu, Y. Q. Yang, J. C. Yu, G. Liu and H. M. Cheng, *Chem. Commun.*, 2014, **50**, 10837–10840.
- 36 L. Ge and C. Han, *Appl. Catal., B*, 2012, **117–118**, 268–274.
- 37 Y. W. Zhang, J. H. Liu, G. Wu and W. Chen, *Nanoscale*, 2012, **4**, 5300–5303.
- 38 J. Theerthagiri, R. A. Senthil, A. Priya, J. Madhavan, R. J. V. Michael and M. Ashokkumar, *RSC Adv.*, 2014, **4**, 38222–38229.
- 39 X. X. Huang, Y. Men, J. G. Wang, W. An and Y. Q. Wang, *Catal. Sci. Technol.*, 2017, **7**, 168–180.
- 40 J. Gangwar, B. K. Gupta, S. K. Tripathi and A. K. Srivastava, *Nanoscale*, 2015, **7**, 13313–13344.
- 41 Y. Xu, H. Xu, L. Wang, J. Yan, H. Li, Y. Song, L. Huang and G. Cai, *Dalton Trans.*, 2013, **42**, 7604–7613.
- 42 B. L. He, B. Dong and H. L. Li, *Electrochem. Commun.*, 2007, **9**, 425–430.
- 43 Q. W. Huang, S. Q. Tian, D. W. Zeng, X. X. Wang, W. L. Song, Y. Y. Li, W. Xiao and C. S. Xie, *ACS Catal.*, 2013, **3**, 1477–1485.
- 44 S. Z. Hu, L. Ma, F. Y. Li, Z. P. Fan, Q. Wang, J. Bai, X. X. Kang and G. Wu, *RSC Adv.*, 2015, **5**, 90750–90756.



- 45 S. Z. Hu, L. Ma, J. G. You, F. Y. Li, Z. P. Fan, G. Lu, D. Liu and J. Z. Gui, *Appl. Surf. Sci.*, 2014, **311**, 164–171.
- 46 K. C. Christoforidis, T. Montini, E. Bontempi, S. Zafeiratos, J. J. D. Jaén and P. Fornasiero, *Appl. Catal., B*, 2016, **187**, 171–180.
- 47 Y. Liu, F. Y. Su, Y. X. Yu and W. D. Zhang, *Int. J. Hydrogen Energy*, 2016, **41**, 7270–7279.
- 48 X. Liu, A. L. Jin, Y. S. Jia, J. Z. Jiang, N. Hu and X. S. Chen, *RSC Adv.*, 2015, **5**, 92033–92041.
- 49 Y. Liu, Y. X. Yu and W. D. Zhang, *Int. J. Hydrogen Energy*, 2014, **39**, 9105–9113.

